

3

4 **Running title:** (-)-Guaiol Targets PPARG in Lung Cancer

5

6 **(-)-Guaiol Inhibits Lung Cancer via PPARG-Dependent Fatty Acid Oxidation**

7

8 Zhen-Yu Zhao<sup>1,#</sup>, Bo Zhang<sup>1,#</sup>, Ying-Bin Luo<sup>1</sup>, Xing-Yu Wang<sup>2</sup>, Yu-Li Wang<sup>1</sup>, Xi Wang<sup>1</sup>, Jian-Hui  
9 Tian<sup>1</sup>, Jian-Chun Wu<sup>1,\*</sup>, Yan Li<sup>1,\*</sup>

10

11 <sup>1</sup>Oncology Department, Shanghai Municipal Hospital of Traditional Chinese Medicine, Shanghai  
12 University of Traditional Chinese Medicine, Shanghai, China; <sup>2</sup>Inner Mongolia Medical University,  
13 Hohhot, Inner Mongolia, China

14

15 \*Correspondence: eq219@163.com; yanli6551@163.com

16

17 #Contributed equally to this work.

18

19 **Received November 11, 2025 / Accepted February 23, 2026**

20

21 The objective of this study was to explore the effect of (-)-guaiol on lung cancer using experimental  
22 validation, mRNA sequencing, and network pharmacology. Potential targets of (-)-guaiol and lung  
23 cancer were identified through SwissTargetPrediction, TCMSP, PharmMapper, OMIM, GeneCards,  
24 and DisGeNET databases. Common targets were analyzed using PPI network, topological screening,  
25 and functional enrichment using STRING, Cytoscape, and Metascape. Molecular docking with core  
26 targets was performed, along with molecular dynamics. In vitro assays (cell counting kit-8 assay,  
27 colony formation, wound healing, Transwell, western blot) and in vivo studies (subcutaneous  
28 xenograft modeling in nude mice, immunohistochemistry, mRNA sequencing) were conducted to  
29 validate the anti-tumor effects and mechanisms of (-)-guaiol compared with the control group.

30 Through multi-database prediction, 153 (-)-guaiol targets and 91 common lung cancer targets were  
31 identified. Protein-protein interaction (PPI) network analysis screened 21 core targets (including  
32 ESR1, EGFR, etc.). GO and KEGG enrichment analyses revealed that these targets are involved in  
33 the regulation of pathways such as fatty acid metabolism. Molecular docking and molecular  
34 dynamics results demonstrated that (-)-guaiol possessed a favorable binding affinity toward the  
35 target proteins SRC, PTGS2, GSK3B, PPARG, ESR1, and HSP90AA1. mRNA sequencing  
36 indicated that the gene expression levels of both PPARG and CD36 were downregulated in lung  
37 cancer tissues of mice treated with (-)-guaiol compared with the control group. Combining the  
38 results of molecular docking, molecular dynamics, and mRNA sequencing, we selected the  
39 PPARG-related signaling pathway for subsequent experiments. Both in vivo and in vitro  
40 experiments validated that (-)-guaiol inhibits lung cancer cell proliferation, invasion, and xenograft  
41 tumor growth in mice by downregulating the PPARG pathway.

42 To conclude, our results demonstrated that (-)-guaiol suppresses lung cancer progression through  
43 downregulation of the fatty acid oxidation-related pathway mediated by PPARG.

44

45 **Key words:** (-)-Guaiol; lung cancer; PPARG; network pharmacology; RNA-sequencing; *in vitro*; *in*  
46 *vivo*

47  
48

49 Lung carcinoma continues to rank among the most prevalent malignancies globally, accounting for  
50 the greatest disease burden, including incidence and mortality rates [1]. Epidemiological studies  
51 show that the five-year survival probability among lung carcinoma cases remains below 20% [2],  
52 and advanced-stage patients exhibit low response rates to conventional chemotherapy and  
53 radiotherapy [3]. Despite advances in targeted therapies (e.g., EGFR inhibitors) and immune  
54 checkpoint blockade (e.g., anti-PD-1/PD-L1), drug resistance and the immunosuppressive tumor  
55 microenvironment persist as significant challenges [4]. Furthermore, the pathological mechanisms  
56 of lung cancer are complex, involving epithelial–mesenchymal transition (EMT), metabolic  
57 reprogramming (such as aberrant fatty acid oxidation), and the tumor-promoting functions of  
58 tumor-associated macrophages (M2-TAMs) [4, 5]. Therefore, exploring novel therapeutic targets  
59 and natural compounds to overcome the limitations of existing treatments is of great significance. In  
60 parallel, recent work has underscored terpenoid natural products as promising sources of multitarget  
61 agents capable of modulating oncogenic signaling and metabolic reprogramming in NSCLC,  
62 supporting further exploration of sesquiterpene scaffolds such as (-)-Guaiol as potential therapeutic  
63 candidates [6, 7].

64 PPARG, as a nuclear hormone receptor a peroxisome proliferator-activated receptor (PPAR) family  
65 member family, it modulates both glucose and lipid metabolism, energy homeostasis, and  
66 inflammatory responses. Increased PPARG expression is associated with poorer survival in breast  
67 cancer mice [8]. PPARG promotes lymph node metastasis of cholangiocarcinoma by upregulating  
68 fatty acid uptake and oxidation through an oleic acid-PPARG-fatty acid binding protein 4 positive  
69 feedback loop [9]. In addition, Tang et al. showed that compared to stage II HCC tissues, high  
70 expression of PPARG in tumor-associated macrophages (TAMs) of stage III HCC tissues  
71 significantly increased fatty acid oxidation [10]. It is noteworthy that PPARG is closely associated  
72 with the polarization of M2 macrophages in the neoplastic cellular milieu, which promote lung  
73 cancer progression via secretion of IL-10 [6]. Therefore, targeting the PPARG-mediated fatty acid  
74 oxidation pathway may represent a novel therapeutic strategy for lung cancer.

75 (-)-Guaiol is a bicyclic sesquiterpene alcohol with a Guaiane-type skeleton that is widely distributed  
76 in the essential oils of several traditional Chinese medicinal plants and coniferous species, and has

77 been reported to exhibit antibacterial and antitumor activities [11]. Structurally, (-)-Guaïol (C<sub>15</sub>H<sub>26</sub>O;  
78 molecular weight 222.37) contains a compact hydrophobic terpene framework bearing a single  
79 hydroxyl group, which confers low aqueous solubility but favorable membrane permeability typical  
80 of lipophilic terpenoids, properties that may influence its cellular uptake and distribution within  
81 tumor tissues. A simplified structural diagram of (-)-Guaïol is provided in Supplementary Figure  
82 S1(The picture is from the Internet). Over the past few years, several studies have started to define  
83 the anticancer profile of (-)-Guaïol in non-small cell lung cancer. Yang et al. showed that (-)-Guaïol  
84 triggers immunogenic cell death in NSCLC, promotes dendritic cell maturation, enhances T-cell  
85 infiltration, and suppresses tumor growth *in vivo* [12]. Cao et al. further reported that (-)-Guaïol  
86 inhibits epithelial–mesenchymal transition in lung cancer by suppressing M2  
87 macrophage- mediated STAT3 signaling, thereby reducing the invasive and migratory capacity of  
88 NSCLC cells [13]. Earlier work also demonstrated that (-)-Guaïol can regulate autophagic cell death  
89 in NSCLC through modulation of mTOR-dependent signaling [14]. Collectively, these studies  
90 indicate that (-)-Guaïol exerts multi- faceted antitumor effects in NSCLC by impacting both tumor  
91 cell- intrinsic survival pathways and the tumor microenvironment. However, it remains unclear  
92 whether (-)-Guaïol mediates anti-lung cancer activity by modulating fatty acid oxidation through  
93 PPARG.

94 Recent advances in network pharmacology have emphasized its interdisciplinary integration and  
95 transcriptomics has provided novel insights for elucidating the multi-target mechanisms of natural  
96 products [7, 15]. Therefore, this study comprehensively applied network pharmacology, RNA  
97 sequencing, and both both laboratory and animal studies to untangle the molecular mechanism  
98 through which (-)-Guaïol inhibits lung cancer through the PPARG-mediated fatty acid  $\beta$ -oxidation  
99 route.

100

## 101 **Materials and Methods**

102 **Screening of (-)-Guaïol and lung cancer target genes.** Supplementary Figure S1 (from the  
103 Internet) displays the molecular structure of (-)-Guaïol. Supplementary Figure S2 illustrates the  
104 complete research workflow. Potential (-)-Guaïol targets were identified using  
105 swissTargetPrediction analysis (<https://www.swisstargetprediction.ch/>), TCMSP  
106 (<https://lsp.nwu.edu.cn/tcmsp.php/>), and PharmMapper server

107 (<https://www.lilab-ecust.co.uk/pharmmapper/>) databases. Concurrently, disease-associated targets  
108 related to lung cancer were retrieved from the OMIM (<https://www.omim.org/>), GeneCards  
109 (<https://www.genecards.org/>), and DisGeNet databases database (<https://www.disgenet.org/>). The  
110 All-potential target proteins were standardized to official gene symbols via  
111 UniProt(<https://www.uniprot.org/>).

112 **Acquisition of potential drug-disease common targets and construction of Venn diagrams.** To  
113 identify the potential therapeutic targets of (-)-Guaioi against lung cancer, the predicted target genes  
114 of (-)-Guaioi and the lung cancer-related disease targets were compared. The intersection targets,  
115 representing the common genes between the drug and the pathological condition, were considered  
116 as potential key targets through which (-)-Guaioi may demonstrate anti-lung cancer efficacy. The  
117 overlapping and unique targets were visualized via a Venn diagram created employing the jVenn  
118 online platform (<https://jvenn.toulouse.inra.fr/app/example.html>), which is part of the SRplot  
119 platform (<https://www.bioinformatics.com.cn/static/others/jVenn/example.html>).

120 **PPI construction and critical target screening.** The STRING database (<https://www.string-db.org>)  
121 was utilized to analyze shared targets and generate a human protein-protein interaction (PPI)  
122 network, with an interaction confidence score cutoff set above 0.4, with isolated nodes excluded  
123 while other parameters retained their default settings. The protein interaction network was  
124 visualized with Cytoscape 3.10.0, followed by node screening based on topological characteristics.  
125 Critical network parameters (degree, betweenness, closeness) identified (-)-Guaioi's primary lung  
126 cancer targets, facilitating development of a drug-target-disease model.

127 **Establishing a "drug-target-pathway-disease" network.** To systematically elucidate the  
128 pharmacological mechanism of (-)-Guaioi against lung cancer, a comprehensive  
129 "drug-target-pathway-disease network was constructed. The network integrates the following key  
130 elements: the drug molecule (-)-Guaioi, the disease (lung cancer), the common potential targets, and  
131 the key signaling pathways. This multi-layered the network visualization and analysis were  
132 performed with Cytoscape (version 3.10.0). Network topology analysis was performed to identify  
133 hub nodes within the network. The Degree centrality, a fundamental metric, was calculated for each  
134 node. The Degree value represents the number of connections a node has, indicating its relative  
135 importance and influence in the network structure. Nodes with a higher Degree value are considered

136 more biologically significant. The size of each node in the visualization was proportional to its  
137 Degree value.

138 **Analysis of GO functions and significant targets for KEGG pathway enrichment.** To  
139 comprehensively elucidate the biological functions and related signaling pathways underlying the  
140 anti-lung cancer effects of (-)-Guaiool, functional enrichment the common targets were analyzed via  
141 Metascape (<https://metascape.org/gp/index.html#/main/step1>). The key targets were analyzed in  
142 Metascape using their official gene symbols, with Homo sapiens designated as the reference species.  
143 The research investigated Gene Ontology (GO) functional annotations-encompassing Biological  
144 Process (BP), Molecular Function (MF), and Cellular Component (CC)-alongside KEGG pathway  
145 analysis enrichment analysis was conducted. The statistical parameters were set as follows: a  
146 p-value cutoff < 0.01, a minimum enrichment count threshold (odds ratio) of 1.5 and a minimal  
147 overlap requirement count (number of genes in a given term) of 3. All enriched terms were ranked  
148 in ascending order of p-value. The twenty most statistically significant enriched terms across gene  
149 ontology and KEGG analyses were selected for visualization. Bar graphs and bubble plots were  
150 created via the online data visualization tool SRplot (<https://www.bioinformatics.com.cn/>).

151 **Molecular docking.** Molecular docking analysis predicted candidate compound-target binding  
152 affinities. The binding affinity, indicated by negative binding energy, demonstrates the stabilization  
153 achieved when the ligand binds to its target protein; more negative values signify greater binding  
154 affinity active compound to the target protein. This investigation, we conducted molecular docking  
155 simulations for (-)-Guaiool targeting the seven highest-ranked core proteins ranked by degree (ESR1,  
156 EGFR, PPARG, PTGS2, HSP90AA1, SRC, and HMGCR). The structures of the small-molecule  
157 drug ligands were acquired retrieved from PubChem (<https://pubchem.ncbi.nlm.nih.gov/>), with  
158 target protein structures obtained from the Protein Data Bank (PDB) (<https://www.rcsb.org/>).  
159 Energy minimization of the ligands was conducted using Chem3D, while the acquired protein  
160 structures were standardized using AutoDockTools 1.5.6, including steps such as hydration and  
161 hydrogen addition. The docking experiments were performed using a blind molecular docking  
162 simulations approach. The Molecular docking was performed to predict binding conformations and  
163 affinities outcomes were visualized and examined using PyMOL software.

164 **Compound Preparation and Vehicle Control.** (-)-Guaiool (purity  $\geq$  99%) was dissolved in DMSO  
165 to prepare a 10 mM stock solution. Working concentrations were prepared by diluting the stock in

166 complete culture medium. All experiments included a vehicle control group treated with 0.1%  
167 DMSO, matching the highest solvent concentration in treated groups.

168 **Cell culture.** The A549 cell line was sourced from the Chinese Academy of Sciences Cell Resource  
169 Center (Shanghai). A549 cells were maintained in high-glucose DMEM medium (KeyGEN  
170 BioTECH, #KGL1206-500) containing 10% fetal bovine serum (FBS; Gibco) with 1%  
171 penicillin-streptomycin, cultured at 37 °C in 5% CO<sub>2</sub>. The experimental manipulations were  
172 generally performed when the cell growth was in the logarithmic phase.

173 **CCK-8 experiments.** Exponentially growing A549 cells were seeded at  $3 \times 10^4$  cells/ml in  
174 96-well plates, followed by medium aspiration after 24 h incubation, and then different  
175 concentration of (-)-Guaiool (C<sub>15</sub>H<sub>26</sub>O, molecular weight: 222.37, purity 99.0%, #HY-N3980,  
176 MedChemExpress, Monmouth Junction, NJ, USA) was added. Following 24 h treatment, the  
177 culture medium was removed, followed by addition of 100 μl 10% CCK-8 solution (#BEB22001,  
178 BEB LABORATORIES, NANJING, China) The compound was dissolved in DMSO, and the final  
179 DMSO concentration in all treatment groups, including the 0 μM control, did not exceed 0.1% (v/v).  
180 Control groups received an equivalent volume of DMSO as vehicle. Each well received an addition,  
181 After a 4 h incubation absorbance at 460 nm was measured at 37 °C. The antiproliferative effect  
182 was calculated using the formula:  $[1 - (\text{treatment OD} / \text{control OD}) \times 100\%$ .

183 **Colony formation assay.** Logarithmically growing A549 Cells were plated in 6-well culture dishes  
184 at 1,000 cells/well, then treated with (-)-Guaiool and maintained under standard conditions (37 °C, 5%  
185 CO<sub>2</sub>) for 10-14 days. When macroscopic cell colonies were clearly visible to the naked eye, The  
186 medium was gently removed by aspiration, followed by two PBS washes of the 6-well plate. Cell  
187 colonies were fixed using 4% paraformaldehyde for 30 minutes under ambient conditions (25 °C).  
188 After fixation, the colonies were incubated using 0.1% (w/v) crystal violet solution for 20 min  
189 under ambient conditions. Following PBS washing and air-drying, the stained colonies were  
190 photographed with a digital camera. The number of colonies (defined as clusters containing > 50  
191 cells) was counted by using ImageJ software.

192 **Wound healing experiments.** Log-phase A549 cells were plated at  $5 \times 10^5$  cells/well in 6-well  
193 plates. Before plating, three horizontal lines were drawn on the outer bottom of each well using a  
194 black marker to serve as reference points for image acquisition. After the cells reached  
195 approximately 80% confluence and were fully adhered, a uniform scratch was created Utilizing a

sterile 200  $\mu$ l micropipette tip, the cell monolayer was treated. Subsequently, the detached cells underwent two PBS washes with gentle agitation before replenishment with (-)-Guaio1-containing fresh medium in each well. The culture plates were then cultured at 37 °C with 5% CO<sub>2</sub>. Photographs of the scratch wounds were obtained at the same predefined locations immediately after scratching (0 h) and after 24 h of incubation.

**Transwell assay.** Cell invasion potential was assessed using a Transwell migration assay. Following matrix polymerization, the lower chamber received 800  $\mu$ l of DMEM containing 10% FBS (Corning #3422, USA) as a chemoattractant, while 200  $\mu$ l cell suspension ( $5 \times 10^4$  cells/ml in serum-free DMEM) was carefully placed in the upper chamber and cultured for 24 h at 37 °C in 5% CO<sub>2</sub>. Subsequently, the inserts were then extracted, the upper membrane's residual non-adherent cells were thoroughly cleared using cotton swabs, while migrated cells adhering to the lower membrane were fixed with 4% paraformaldehyde for 10 min, PBS-washed twice, and allowed to air-dry prior to 10 min staining with 0.1% crystal violet. Following drying at ambient temperature, Photographs of the invaded cells were taken using an inverted microscope (LEIC ,MZ-10F, German) for subsequent quantification.

**Western blot.** After treatment with (-)-Guaio1, Cell lysates were generated with ice-cold RIPA buffer supplemented with phosphatase and protease inhibitors (1:1:50). Protein quantification was performed with the BCA Protein Quantification Kit (#PA115, TIANGEN, Beijing, China). Protein samples (50  $\mu$ g/lane) were electrophoresed by SDS-PAGE and electroblotted onto PVDF membranes (#356234, Corning, USA) using following wet transfer, membranes were blocked with 5% skim milk and subsequently probed with primary antibodies overnight at 4 °C incubation, specifically: PPAR $\gamma$  (1:1000, #YM1082, ImmunoWay, USA), CPT1A (1:1000, #22170-1-AP, Proteintech), CPT1B (1:1000, #15184-1-AP, Proteintech), CD36 (1:1000, #28109, Proteintech), and  $\beta$ -ACTIN (1:3000). Subsequently, membranes were incubated with HRP-conjugated secondary antibody (1:10,000, #66009, Proteintech, Wuhan, China) Subsequently, the membranes were treated with HRP-linked secondary antibody (1:10,000, #SA00001, Proteintech) at ambient temperature for 1 h, followed by ECL visualization and ImageJ quantification of protein bands.

**Animal modeling.** All procedures involving animals complied with NIH animal care standards and received approved by the Ethics Committee of experimental animal medicine of Shanghai Hospital of traditional Chinese Medicine (Approval No. 2023047). Optimally proliferating A549 cells were

226 selected and implanted subcutaneously ( $3 \times 10^4$  cells/mouse) in the right scapular area using  
227 6-week-old Balb/c nude mice (Shanghai Jima Pharmaceutical Technology Co., Ltd.). Drug  
228 treatment commenced 72 h post-inoculation: the control cohort was administered intraperitoneal  
229 injections of physiological saline solution (100  $\mu$ l) every two days. In contrast, the experimental  
230 cohort was subjected to intraperitoneal injections of 8 mg/kg (-)-Guaiol (100  $\mu$ l) every two days.  
231 The operational procedure is illustrated in Supplementary Figure S3 (figure created via  
232 <https://BioRender.com>). Tumor progression in xenograft-bearing mice was tracked daily, recording  
233 growth parameters (size, mass, volume) and latency period from implantation to tumor  
234 establishment. Following a three-week period, the animals were euthanized via cervical dislocation,  
235 after which tumors were excised by blunt dissection, weighed, and volumetrically measured. Partial  
236 tumor tissues were collected for mRNA sequencing and immunohistochemical experiments.

237 **Immunohistochemistry.** After three weeks, the animals were euthanized via cervical dislocation,  
238 followed by tumor excision through blunt dissection, weighing, and volume measurement. Three  
239 weeks post-treatment, animals were euthanized via cervical dislocation, followed by tumor excision  
240 through blunt dissection with subsequent weighing and volumetric measurement. After overnight  
241 primary antibody incubation at 4 °C, the tissue sections were incubated with HRP-conjugated  
242 secondary antibodies for 30 min under ambient conditions. DAB was used for chromogenic  
243 detection, followed by hematoxylin counterstaining, differentiation, and bluing. Finally, the tissue  
244 sections were dehydrated, cleared, and mounted with neutral balsam before microscopic imaging  
245 for quantitative assessment of positively stained regions.

246 **mRNA sequencing.** mRNA sequencing (mRNA-seq) is a high-throughput gene expression  
247 profiling technique capable of untangling differences in gene expression profiles across various  
248 cells or tissues in both breadth and depth, as well as detecting splicing variants generated by RNA  
249 catalysis. In recent years, this technology has achieved significant advancements and has been  
250 widely adopted. Compared to conventional genetic testing methods, mRNA-seq offers multiple  
251 advantages. In this experiment, six samples from both the control and experimental groups were  
252 preserved on dry ice and subsequently sent to Ouyi Biotechnology Co., Ltd. (Shanghai, China).  
253 Following a three-week period, the animals were euthanized via cervical dislocation, after which  
254 tumors were excised by blunt dissection, weighed, and volumetrically measured. Following quality  
255 evaluation of raw sequencing data, the filtered Reads were aligned to the reference genome.

256 Differentially expressed genes (DEGs) were determined by applying cutoff criteria of  $|\log_2FC| > 1$   
257 and  $q\text{-value} < 0.05$ .

258 **Statistical analysis.** GraphPad Prism 8.0.2 was used to evaluate all experimental data. Each  
259 experiment was carried out at least three times. The Shapiro-Wilk test was used to determine  
260 whether the experimental data satisfied normal distribution. Data that met normal distribution were  
261 analyzed for differences between groups using one-way ANOVA. Data that did not satisfy normal  
262 distribution were analyzed using Kruskal-Wallis analysis. Significant differences were defined as  $p$   
263  $< 0.05$ .

264

## 265 **Results**

266 **(-)-Guaiool and the acquisition of potential targets in lung cancer.** The SwissTargetPrediction  
267 database identified 40 potential (-)-Guaiool targets, the TCMSP database contained 13 targets of  
268 (-)-Guaiool, and the PharmMapper database identified 110 targets of (-)-Guaiool. After removing  
269 duplicates, a compilation of 153 potential targets for (-)-Guaiool was assembled. Additionally, a total  
270 of 446 lung cancer-related targets were obtained from the OMIM database; the GeneCards database  
271 identified 25,001 potential targets associated with lung carcinoma; the DisGeNET database  
272 additionally identified 4,173 targets linked to lung cancer. Comparative analysis of both target sets  
273 revealed 91 common targets between (-)-Guaiool and lung cancer, visualized through a Venn  
274 diagram (Figure 1A).

275 **PPI network of the common targets between (-)-Guaiool and lung cancer.** The 91 common  
276 targets identified for (-)-Guaiool and lung cancer were analyzed for protein-protein interactions using  
277 the STRING database (<https://www.string-db.org>) and visualized through Cytoscape 3.10.0. Finally,  
278 the interaction network between (-)-Guaiool and lung cancer targets was constructed. Degree values  
279 determined the nodes' size and color. There were a total of 90 nodes (representing 90 screened  
280 potential shared targets) and 418 edges (Highlighting interconnections among 90 prospective shared  
281 targets), as depicted in Figure 1B.

282 **Screening and visualization of key targets.** Based on the analysis of node topological properties,  
283 the included data comprised node degree, betweenness centrality (BC) along with proximity  
284 centrality (PC). The screening criteria were set as follows: node degree  $\geq 10$ , betweenness centrality  
285  $\geq 0.017$ , and closeness centrality  $\geq 0.4$ . Twenty-one potential key targets were identified, indicating

286 their likely role in mediating (-)-Guaio'l's anti-lung cancer effects. Supplementary Table S1 presents  
287 the gene names, node degrees, betweenness centrality, and closeness centrality of these key targets.  
288 Figure 1C illustrates the interaction network of core targets. The seven highest-ranked targets based  
289 on node degree were: ESR1 (degree = 33), EGFR (degree=32), PPARG (degree=31), PTGS2  
290 (degree=29), HSP90AA1 (degree=29), SRC (degree=25), and HMGCR (degree=24).

291 **GO and KEGG functional enrichment analysis.** The 21 core target genes were analyzed using  
292 Metascape for Gene Ontology (GO) term enrichment analysis. The GO functional analysis revealed  
293 22 cellular component, 39 molecular functions and 507 biological processes. The top 20  
294 highest-degree nodes from each category were selected for analysis, and the findings were  
295 displayed as histograms (Figure 2A) and bubble plots (Figure 2B). The 20 most highly enriched  
296 biological processes were: response to hormone, Nuclear receptors meta pathway, modulation of  
297 protein localization establishment, Cancer pathways, Downregulation of intracellular signal  
298 transduction, Regulation of systemic processes, Modulation of protein trafficking, Regulation of the  
299 MAPK cascade, Cellular response to hormonal stimuli, modulation of inflammatory reactions and  
300 suppression of apoptosis-related signaling cascades, upregulation of proteins transport, CKAP4  
301 signaling pathway map, here is a professionally rewritten version with precise terminology and  
302 improved academic style, regulation of miRNA transcription, regulation of ncRNA transcription,  
303 Relationship between inflammation COX 2 and EGFR, Aryl hydrocarbon receptor pathway, PID  
304 AR TF PATHWAY. The first 20 cells were composed of vesicle lumen, glutamatergic synapse,  
305 membrane microdomain, dendritic tree, membrane raft, dendrite, axon, ficolin-1-rich granule lumen,  
306 distal axon, apical part of cell, cytoplasmic vesicle lumen, cell body, receptor complex,  
307 ficolin-1-rich granule, neuronal cell body, secretory granule lumen, cell projection membrane,  
308 endocytic vesicle, nuclear speck, early endosome. The twenty most significantly enriched molecular  
309 functions encompassed RNA polymerase II-specific DNA-binding transcriptional regulation by  
310 protein kinases functionality, protein kinase association, kinase interaction, kinase catalytic activity,  
311 The enriched molecular functions comprised DNA-binding transcription factor interaction,  
312 phosphotransferase activity, transcription factor binding, alcohol group acceptor function,  
313 phosphatase association, protein domain-specific binding, transcription coregulator engagement,  
314 ligand-activated transcription factor function, ATPase association, tetrapyrrole binding, heme  
315 interaction, protein phosphatase binding, nuclear receptor function, transcription coactivator

316 engagement, nitric-oxide synthase regulation, and fatty acid binding.  
317 Twenty-one key targets were analyzed in Metascape for KEGG pathway enrichment, resulting in 45  
318 significant signaling pathways. The top 20 KEGG pathways ranked by degree centrality were  
319 mapped and visualized as bubble plots (Figure 2C). The KEGG pathways and their associated  
320 targets are annotated in Supplementary Table S2. The 20 most enriched KEGG pathways were:  
321 Proteoglycans in cancer, Fluid shear stress in atherosclerosis, receptor-mediated chemical  
322 carcinogenesis, Oncogenic pathways, Lipid metabolism in atherosclerosis, Prostatic carcinoma,  
323 Cytomegalovirus infection in humans, Resistance to EGFR tyrosine kinase inhibitors, VEGF  
324 Signaling cascade, Prolactin-mediated signaling, Estrogen-mediated signaling, Non-alcoholic  
325 steatohepatitis, kaposi sarcoma-associated herpesvirus infection, Hepatocellular carcinoma, Focal  
326 adhesion, Alcoholic liver disease, Endocrine resistance, Diabetic cardiomyopathy, The IL-17 and  
327 PI3K-Akt signaling cascades were visualized using Cytoscape software version 3.10.0 of (-)-Guaioi  
328 with 21 key targets, Top20 signaling pathway and lung cancer, as shown in Figure 3.

329 **Molecular docking and Molecular dynamics.** Binding of simulated drugs and disease targets were  
330 detected by molecular docking (Figures 4A-4G). Supplementary Table S3 shows the binding energy  
331 of (-)-Guaioi to each key target. The results showed that (-)-Guaioi bound well to all key targets,  
332 with the strongest binding to GSK3B, followed by SRC, ESR1, PTGS2, PTGS2, PPARG,  
333 HSP90AA1, and EGFR. The molecular docking showed that (-)-Guaioi may elicit its anti-lung  
334 cancer effect by targeting these proteins.

335 Structural stability in protein-ligand systems was assessed using root-mean-square deviation  
336 (RMSD), with lower values indicating greater complex stability, as illustrated in Figure 5A, except  
337 for the EGFR-(-)-Guaioi complex, the RMSD values of the complexes formed between SRC,  
338 PTGS2, GSK3B, PPARG, ESRI, and HSP90AA1 with (-)-Guaioi reached equilibrium after 5 ns,  
339 eventually stabilizing at approximately 2.3 Å, 2.4 Å, 1.8 Å, 2.8 Å, 2.5 Å, and 4.7 Å, respectively,  
340 indicating high stability of these complexes. Evaluation of the gyration radius (Rg) (Figure 5B)  
341 revealed minor structural fluctuations during the simulation, with no significant expansion or  
342 contraction observed. The solvent-accessible surface area (SASA) (Figure 5C) further indicated no  
343 substantial change in surface area after binding, suggesting that ligand binding had limited impact  
344 on protein conformation. Hydrogen bond analysis (Figure 5D) demonstrated that stable hydrogen  
345 bond interactions were maintained between (-)-Guaioi and each target protein, with the number of

346 bonds mostly ranging between one and two, and occasionally reaching three, indicating favorable  
347 binding specificity. Moreover, the root mean square fluctuation (RMSF) results (Figure 5E) showed  
348 that residue fluctuations in all complexes were mostly below 3 Å, suggesting low overall structural  
349 flexibility and high stability.

350 Subsequently, the binding free energy of ligand-protein complexes was computed using the  
351 MM/PBSA approach using its bound conformation (Figure 6A). This study further computed and  
352 analyzed the amino acid residues that contributed significantly to the binding of the small molecule  
353 within each complex system. The results indicated that in the SRC-(-)-GuaioI complex, residues  
354 LEU407, ILE336, LEU325, LYS295, and MET314 exhibited high contribution values (Figure 6B).  
355 In the ESR1-(-)-GuaioI complex, residues ILE424, MET421, LEU387, ALA350, MET388, LEU391,  
356 LEU428, and LEU525 showed high contribution values (Figure 6C). For the GSK3B-(-)-GuaioI  
357 complex, residues PHE229, TYR288, and ILE228 were identified with high contribution values  
358 (Figure 6D). In the PTGS2-(-)-GuaioI complex, residues LEU152, ARG469, GLN461, PRO153,  
359 and ASN39 demonstrated high contribution values (Figures 6E, 6F). In the PPARG-(-)-GuaioI  
360 complex, residues SER429 and LEU431 were found to have high contribution values (Figure 6G).  
361 Lastly, in the HSP90AA1-(-)-GuaioI complex, residues MET998, ASN51, PHE138, LEU107,  
362 ASN106, and ALA55 showed high contribution values (Figure 6H). These results indicate that  
363 these residues might be crucial for catalysis.

364 In summary, the complex systems of SRC-(-)-GuaioI, PTGS2-(-)-GuaioI, GSK3B-(-)-GuaioI,  
365 PPARG-(-)-GuaioI, ESR1-(-)-GuaioI, and HSP90AA1-(-)-GuaioI all exhibited stable binding  
366 conformations, with robust hydrogen bond interactions observed in each complex. These results  
367 indicate that the small molecule (-)-GuaioI possesses favorable binding affinity toward the target  
368 proteins SRC, PTGS2, GSK3B, PPARG, ESR1, and HSP90AA1.

369 **mRNA Sequencing.** Through mRNA sequencing analysis of lung cancer tissues from the control  
370 and experimental groups (n = 3), a total of 24,443 genes expressed in at least one sample were  
371 identified, gene expression analysis detected 22,609 transcripts in controls versus 22,692 in treated  
372 samples, with differential expression analysis identifying 49 upregulated and 84 downregulated  
373 genes relative to controls. Comparative analysis revealed downregulated expression of both PPARG  
374 and CD36 genes in (-)-GuaioI-treated murine lung cancer tissues relative to controls (Figure 7A).  
375 The PPARG the signaling pathway was pinpointed as a pivotal pathway mediating (-)-GuaioI

376 inhibits lung cancer (Figure 7B). GO analysis further indicated that (-)-Guaiol can inhibit  
377 triglyceride lipase activity (Figure 7C). Based on these findings, we speculate that (-)-Guaiol may  
378 suppress lung cancer by downregulating PPARG signaling pathway-mediated fatty acid oxidation.

379 **(-)-Guaiol inhibits cell proliferation and invasion ability of lung cancer cells.** Cell viability of  
380 (-)-Guaiol-treated A549 cells was evaluated using the CCK-8 method (Figure 8A). The findings  
381 indicated that the concentration of (-)-Guaiol required to inhibit  
382 cell viability by 50% was 80.73  $\mu\text{M}$ . At concentrations ranging from 10  $\mu\text{M}$  to 40  $\mu\text{M}$ , (-)-Guaiol  
383 showed no significant cytotoxicity toward A549 cells. (-)-Guaiol markedly inhibited PPARG  
384 expression and its downstream targets (CPT1A, CPT1B, CD36) at the proteomic level in A549 cells  
385 (Figure 8B). At 10  $\mu\text{M}$  and 30  $\mu\text{M}$  concentrations, (-)-Guaiol substantially suppressed A549 cell  
386 proliferation, migration, and invasion (Figures 8C-8E).

387 To verify the generality of (-)-Guaiol's effects, we performed additional experiments in H1299 cells  
388 (another NSCLC cell line). The CCK-8 assay showed that (-)-Guaiol inhibited H1299 cell viability  
389 (Figure 8A). Western blot analysis further confirmed that (-)-Guaiol downregulated the expression  
390 of PPARG and its downstream targets (CPT1A, CPT1B, CD36) in H1299 cells, consistent with the  
391 results in A549 cells (Figure 8B). These data indicate that (-)-Guaiol's inhibitory effect on NSCLC  
392 cells via the PPARG pathway is not cell line-specific.

393 **(-)-Guaiol inhibits the growth of transplanted tumors in lung cancer subcutaneous xenograft**  
394 **mice.** Following the conclusion of the experiment, the mice underwent euthanasia, and  
395 subcutaneous tumor tissues were dissected and photographed (Figure 9A). Mean body weights were  
396  $22.76 \pm 0.55$  g (control) and  $22.58 \pm 0.33$  g (experimental), showing no significant intergroup  
397 difference ( $p > 0.05$ , Figure 9B). (-)-Guaiol significantly inhibited tumor volume and weight  
398 ( $1720.01 \pm 246.94$  mm<sup>3</sup> vs.  $688.828 \pm 146.60$  mm<sup>3</sup> (Figure 9C);  $1.35 \pm 0.08$  g vs.  $0.97 \pm 0.03$  g (Figure  
399 9D)). Furthermore, (-)-Guaiol markedly suppressed the protein expression of PPARG, CPT1A,  
400 CPT1B, and CD36 in the subcutaneous xenograft tumor tissues (Figure 9E).

401

## 402 Discussion

403 Through network pharmacological screening, we identified 91 potential common targets. The top 21  
404 in degree value were ESR1, EGFR, PPARG, PTGS2, HSP90AA1, SRC, GSK3B, PPARA, HMGCR,  
405 MAPK14, CYP19A1, KDR, AR, PTPN1, REN, GSTP1, TERT, FABP1, CHEK1, CYP2C19, and

406 CHRM2. There is a high probability that these targets are key targets for therapeutic potential of  
407 (-)-Guaiol in lung carcinoma treatment.

408 PPI analysis revealed that the primary targets of (-)-Guaiol in the therapy of pulmonary carcinoma  
409 include ESR1, EGFR, PPARG, PTGS2, HSP90AA1, SRC, and HMGCR. Among these, estrogen  
410 receptor 1 (ESR1) was identified as the key target with the highest degree of connectivity. Previous  
411 research revealed significantly higher ESR1 methylation levels in peripheral blood from NSCLC  
412 patients compared to controls, indicating its possible application as an early detection marker for  
413 lung cancer [16]. Research indicates that ESR1 genetic variants may regulate bisphenol A  
414 elimination through urine, subsequently affecting lung cancer cell motility and tumor advancement  
415 [17]. Epidermal growth factor receptor (EGFR) expression demonstrates a significant association  
416 with lung cancer progression and unfavorable prognosis, serving as a critical driver in NSCLC. In  
417 particular, activation of mutant EGFR and its inhibition by specific tyrosine kinase inhibitors (TKIs)  
418 can elicit significant tumor responses [18, 19]. EGFR supports the survival and physiological roles  
419 of cancer stem cells (CSCs), encompassing stem-like properties maintenance, metabolic regulation,  
420 immune-regulatory functions, quiescence, and chemoresistance [20]. Numerous Research has  
421 demonstrated that PPARG activation can potently suppress NSCLC proliferation and induce  
422 apoptosis [21-23]. However, some studies have also reported that PPARG expression may promote  
423 lung cancer growth and invasion. PPARG has been shown to alleviate the inhibitory effect of  
424 transforming growth factor-beta (TGF $\beta$ ) on mitosis in H460 cells [24]. Additionally, PPARG can  
425 promote tumor angiogenesis and alter the tumor microenvironment, thereby facilitating the  
426 generation of regulatory T cells (Tregs) [9, 25]. Overexpression of PTGS2 induces abundant  
427 secretion of exosomal miR-1290, which promotes the activation of cancer-associated fibroblasts  
428 and tumor growth in lung adenocarcinoma via the CUL3-Nrf2 pathway [26]. A recent study  
429 discovered that  $\beta$ 5-integrin can activate tumor cell pyroptosis through the SRC signaling pathway,  
430 thereby reversing radiation resistance in lung cancer patients [27]. Furthermore, AMPK may  
431 enhance anti-tumor immune responses by suppressing PD-1 in regulatory T cells [28].

432 GO and KEGG analyses revealed multiple potential mechanisms and the mechanisms by which  
433 (-)-Guaiol potentially influences its outcomes in lung cancer treatment. GO analysis suggested that  
434 (-)-Guaiol may influence lung cancer progression via various biological processes, including  
435 inflammatory response, apoptosis, CKAP4 signaling pathway, and gastrin signaling pathway.

436 KEGG analysis revealed additional signaling pathways, notably VEGF, PI3K-Akt, and IL-17  
437 cascades. Previous research indicates (-)-Guaiool can inhibit lung adenocarcinoma cell proliferation  
438 and induce apoptosis through PI3K/Akt signaling [29]. The VEGF family, which comprises six  
439 major isoforms (VEGF121, VEGF145, VEGF165, VEGF183, VEGF189, and VEGF206), is  
440 involved in tumor angiogenesis. However, certain VEGF-A isoforms may be expressed through an  
441 inhibitory signaling pathway, leading to the arrest of endothelial cell migration and proliferation,  
442 thereby exerting an anti-angiogenic effect [30]. The precise mechanism underlying this process  
443 remains unclear. The role of the IL-7 signaling pathway in lung cancer has been extensively studied.  
444 Current research indicates that IL-7 downregulates autophagy in NSCLC through the P53-mediated  
445 AMPK/mTOR cascade [31]. Additionally, IL-7 signaling through the IL-7R-JAK3/STAT5 axis has  
446 been shown to enhance chemoresponsiveness in NSCLC cells [32].

447 Molecular docking studies revealed that (-)-Guaiool exhibits varying binding affinities to the  
448 screened key targets, with the highest affinity observed for GSK3B. Thus, GSK3B, the mRNA form  
449 of GSK-3 $\beta$ , may be a key target of (-)-Guaiool in the treatment of lung cancer. One study found that  
450 circular RNA circ-GSK3B enhances GSK3 $\beta$  expression by competitively adsorbing miR-3909 and  
451 miR-3681-3p, thereby inhibiting the proliferation and motility of lung carcinoma cells [33].  
452 Multiple studies have also reported that various other drugs or factors can influence lung cancer  
453 cells via GSK-3 $\beta$ . Diosgenin inhibits the proliferation, invasion, as well as the EMT in lung  
454 adenocarcinoma mediated by the AKT/GSK3 $\beta$ /mTOR pathway cascade [34]. Astragaloside IV  
455 inhibits NSCLC progression through suppression of the AKT/GSK-3 $\beta$ / $\beta$ -catenin pathway [35]. The  
456 lncRNA LINC00222 regulates GSK3 $\beta$  function and enhances apoptosis in NSCLC cells [36].  
457 Deguelin inhibits non-small cell lung cancer advancement by disrupting EGFR transduction and  
458 enhancing GSK3 $\beta$ /FBW7-dependent Mcl-1 proteolysis [37]. Additionally, the interaction between  
459 PCNA and GSK3 $\beta$  regulates the apoptosis process in H1299 lung cancer cells [38]. Through mRNA  
460 sequencing, we observed that (-)-Guaiool downregulates the gene expression of PPARG and CD36,  
461 which is consistent with the network pharmacology analysis identifying PPARG as a key target of  
462 (-)-Guaiool in lung cancer treatment. Notably, PPARG is not an isolated target but is functionally  
463 linked to the PI3K/Akt/mTOR signaling axis. Evidence indicates that PPARG enables the  
464 PI3K/Akt/mTOR (PAM) pathway by facilitating fatty acid synthase (FASN) activity, leading to  
465 significant upregulation of p-mTOR (Ser2481 and Ser2448), PI3K (p85), p-AKT, and p-4EBP1

466 upon PPARG overexpression [39]. Conversely, PPARG knockdown downregulates these key  
467 signaling molecules [39]. Importantly, mTOR inhibition (e.g., with Everolimus) has been shown to  
468 significantly weaken or abolish the proliferative advantage conferred by PPARG overexpression,  
469 demonstrating that PAM pathway activation is central to PPARG-mediated resistance [39]. Given  
470 that (-)-Guaiool has previously been reported to regulate autophagic cell death via mTOR signaling  
471 in NSCLC [14], our current findings suggest that PPARG downregulation may represent an  
472 upstream mechanism contributing to mTOR inhibition. Thus, (-)-Guaiool may exert its anti-tumor  
473 effects through a coordinated suppression of metabolic (PPARG-mediated fatty acid oxidation) and  
474 proliferative (PI3K/Akt/mTOR) pathways, extending its previously reported actions on RAD51 and  
475 mTOR. Further investigations demonstrated that (-)-Guaiool downregulates the PPARG signaling  
476 pathway and inhibits the activity of triglyceride lipase. Therefore, we postulate that (-)-Guaiool's  
477 antitumor activity may involve PPARG regulation, subsequently influencing fatty acid  
478 oxidation-associated genes including CPT1A, CD36, and CPT1B.

479 To verify these observations and hypotheses, we performed corresponding *in vitro* and *in vivo*  
480 studies. Notably, the anti-tumor effects of (-)-Guaiool were validated in two NSCLC cell lines (A549  
481 and H1299), with consistent downregulation of the PPARG-mediated fatty acid oxidation pathway  
482 and inhibition of cell viability. This consistency across different NSCLC cell lines strengthens the  
483 generality of our findings, supporting that (-)-Guaiool's mechanism is not restricted to a single cell  
484 type. *In vitro* analyses revealed (-)-Guaiool's suppression of PPARG expression and modulation of  
485 downstream effectors (CPT1A, CPT1B, CD36) in lung cancer cells. Results from Transwell assays,  
486 wound healing assays. Colony formation assays demonstrated that (-)-Guaiool significantly inhibited  
487 invasive capacity, migration, and proliferation capabilities of lung cancer cells. Meanwhile, *in vivo*  
488 animal experiments also revealed that (-)-Guaiool inhibited the growth of transplanted Lewis lung  
489 carcinoma tumors in mice. Furthermore, immunohistochemical results showed that (-)-Guaiool  
490 significantly suppressed the expression of PPARG and its downstream pathway  
491 components-CPT1A, CPT1B, and CD36-in lung cancer tissues. After clarifying the correlation  
492 between (-)-Guaiool and the fatty acid oxidation process in lung cancer, as well as its molecular  
493 mechanism of action, we illustrated a schematic diagram of (-)-Guaiool-mediated regulation of fatty  
494 acid oxidation in lung cancer in Figure 10 (Created with BioGDP.com [40]).

495 However, this study still has the following limitations. First, the differential roles of PPAR $\gamma$  in  
496 tumor cells and stromal cells require further validation through more precise cell-specific knock-out  
497 experiments. Second, the relationship between fatty acid oxidation inhibition and the function of  
498 immune effector cells warrants further investigation. Finally, the pharmacokinetic characteristics of  
499 (-)-Guaiool require validation in larger cohorts.

500 In conclusion, through integrated network pharmacology, molecular dynamics, transcriptomic  
501 analysis, and experimental validation, this study reveals (-)-Guaiool's potent suppression of lung  
502 cancer cell invasion, migration and proliferation via PPAR $\gamma$ -mediated fatty acid metabolism. The  
503 compound exhibits polypharmacological activity targeting multiple pathways including  
504 ESR1/GSK3 $\beta$ /PPAR $\gamma$  signaling, lipid metabolism, inflammation, apoptosis, and  
505 IL-17/VEGF/PI3K-Akt axes.

506

507 Acknowledgements: This work was supported by Shanghai University of Traditional Chinese  
508 Medicine Science and Technology Development Project (24KFL090); The National Natural  
509 Science Foundation of China (No.82204842, No.82174183, No.82575159); The YangFan project  
510 from the Science and Technology Commission of Shanghai Municipality (No. 22YF1445400);  
511 Shanghai Three-year Action Plan to Further Accelerate the Development of Traditional Chinese  
512 Medicine Inheritance and Innovation (2021-2023) (No. ZY(2021-2023)-0211) and Shanghai  
513 famous old Chinese medicine academic experience research studio construction project (No.  
514 SHGZS-202210).

515

516 **Supplementary data are available in the online version of the paper.**

517

518

## 519 **References**

- 520 [1] BRODY H. Lung cancer. *Nature* 2020; 587: S7.  
521 <https://doi.org/10.1038/d41586-020-03152-0>
- 522 [2] WEI X, PNG CW, WEERASOORIYA M, LI H, ZHU C et al. Tumor Promoting Function of  
523 DUSP10 in Non-Small Cell Lung Cancer Is Associated With Tumor-Promoting Cytokines.  
524 *Immune Netw* 2023; 23: e34. <https://doi.org/10.4110/in.2023.23.e34>
- 525 [3] MAHARATI A, MOGHBELI M. Role of microRNAs in regulation of doxorubicin and  
526 paclitaxel responses in lung tumor cells. *Cell Div* 2023; 18: 11.  
527 <https://doi.org/10.1186/s13008-023-00093-8>

- 528 [4] WANG F, YANG M, LUO W, ZHOU Q. Characteristics of tumor microenvironment and  
529 novel immunotherapeutic strategies for non-small cell lung cancer. *J Natl Cancer Cent* 2022;  
530 2: 243-262. <https://doi.org/10.1016/j.jncc.2022.10.002>
- 531 [5] HU T, HAN F, AN Z. Comprehensive profiling of serum glycosphingolipids to discover the  
532 diagnostic biomarkers of lung cancer and uncover the variation of glycosphingolipid  
533 networks in different lung cancer subtypes. *Anal Methods* 2024; 16: 7873-7887.  
534 <https://doi.org/10.1039/d4ay01685h>
- 535 [6] ZHANG J, TANG M, SHANG J. PPAR $\gamma$  Modulators in Lung Cancer: Molecular  
536 Mechanisms, Clinical Prospects, and Challenges. *Biomolecules* 2024; 14: 190.  
537 <https://doi.org/10.3390/biom14020190>
- 538 [7] MANGRAL ZA, BHAT BA, SHEIKH S, ISLAM SU, TARIQ L et al. Exploring the  
539 therapeutic potential of *Rhododendron anthopogon* D. Don essential oil constituents against  
540 lung cancer: A network pharmacology-based analysis with molecular docking and  
541 experimental studies. *Comput Biol Med* 2025; 187: 109827.  
542 <https://doi.org/10.1016/j.compbimed.2025.109827>
- 543 [8] YANG PB, HOU PP, LIU FY, HONG WB, CHEN HZ et al. Blocking PPAR $\gamma$  interaction  
544 facilitates Nur77 interdiction of fatty acid uptake and suppresses breast cancer progression.  
545 *Proc Natl Acad Sci U S A* 2020; 117: 27412-27422.  
546 <https://doi.org/10.1073/pnas.2002997117>
- 547 [9] ZHANG H, ZHU K, ZHANG R, GUO Y, WANG J et al. Oleic acid-PPAR $\gamma$ -FABP4 loop  
548 fuels cholangiocarcinoma colonization in lymph node metastases microenvironment.  
549 *Hepatology* 2024, 80: 69-86. <https://doi.org/10.1097/HEP.0000000000000784>
- 550 [10] TANG W, SUN G, JI GW, FENG T, ZHANG Q et al. Single-cell RNA-sequencing atlas  
551 reveals an FABP1-dependent immunosuppressive environment in hepatocellular carcinoma.  
552 *J Immunother Cancer* 2023; 11: e007030. <https://doi.org/10.1136/jitc-2023-007030>
- 553 [11] CHOUDHARY MI, BATOOL I, ATIF M, HUSSAIN S, ATTA UR R. Microbial  
554 transformation of (-)-guaiol and antibacterial activity of its transformed products. *J Nat Prod*  
555 2007; 70: 849-852. <https://doi.org/10.1021/np068052a>
- 556 [12] YANG X, YANG J, GU X, TAO Y, JI H et al. (-)-Guaiol triggers immunogenic cell death  
557 and inhibits tumor growth in non-small cell lung cancer. *Mol Cell Biochem* 2023; 478:  
558 1611-1620. <https://doi.org/10.1007/s11010-022-04613-y>
- 559 [13] CAO Y, WU Y, TU H, GU Z, YU F et al. (-)-Guaiol inhibit epithelial-mesenchymal  
560 transition in lung cancer via suppressing M2 macrophages mediated STAT3 signaling  
561 pathway. *Heliyon* 2023; 9: e19817. <https://doi.org/10.1016/j.heliyon.2023.e19817>
- 562 [14] YANG X, ZHU J, WU J, HUANG N, CUI Z et al. (-)-Guaiol regulates autophagic cell death  
563 depending on mTOR signaling in NSCLC. *Cancer Biol Ther* 2018; 19: 706-714.  
564 <https://doi.org/10.1080/15384047.2018.1451277>
- 565 [15] TAN B, LAN X, ZHANG Y, LIU P, JIN Q et al. Effect of 23- hydroxybetulinic acid on lung  
566 adenocarcinoma and its mechanism of action. *Exp Ther Med* 2024; 27: 239.  
567 <https://doi.org/10.3892/etm.2024.12527>
- 568 [16] FAN XP, DOU CY, FAN YC, CAO CJ, ZHAO ZH et al. Methylation status of the estrogen  
569 receptor 1 promoter predicts poor prognosis of acute-on-chronic hepatitis B liver failure.  
570 *Rev Esp Enferm Dig* 2017; 109: 818-827. <https://doi.org/10.17235/reed.2017.4426/2016>
- 571 [17] LI J, JI Z, LUO X, LI Y, YUAN P et al. Urinary bisphenol A and its interaction with ESR1  
572 genetic polymorphism associated with non-small cell lung cancer: findings from a

- 573 case-control study in Chinese population. *Chemosphere* 2020, 254: 126835.  
574 <https://doi.org/10.1016/j.chemosphere.2020.126835>
- 575 [18] CHENG FJ, CHEN CH, TSAI WC, WANG BW, YU MC et al. Cigarette smoke-induced  
576 LKB1/AMPK pathway deficiency reduces EGFR TKI sensitivity in NSCLC. *Oncogene*  
577 2021; 40: 1162-1175. <https://doi.org/10.1038/s41388-020-01597-1>
- 578 [19] TESSEMA M, ROSSI MR, PICCHI MA, YINGLING CM, LIN Y et al. Common  
579 cancer-driver mutations and their association with abnormally methylated genes in lung  
580 adenocarcinoma from never-smokers. *Lung Cancer* 2018; 123: 99-106.  
581 <https://doi.org/10.1016/j.lungcan.2018.07.011>
- 582 [20] XU Z, QIN F, YUAN L, WEI J, SUN Y et al. EGFR DNA Methylation Correlates With  
583 EGFR Expression, Immune Cell Infiltration, and Overall Survival in Lung Adenocarcinoma.  
584 *Front Oncol* 2021; 11: 691915. <https://doi.org/10.3389/fonc.2021.691915>
- 585 [21] TU H, FENG Y, WANG W, ZHOU H, CAI Q et al. Exploring the mechanism of bioactive  
586 components of *Prunella vulgaris* L. in treating hepatocellular carcinoma based on network  
587 pharmacology. *Chem Biol Drug Des* 2024; 103: e14413. <https://doi.org/10.1111/cbdd.14413>
- 588 [22] ZHOU S, WANG Y, XIE M, LI J, MENG P et al. Uncovering the antidepressant active  
589 ingredients and related molecular mechanisms of Xiaoyao Pill using integrated  
590 pharmacological strategy. *J Chromatogr B Analyt Technol Biomed Life Sci* 2025; 1255:  
591 124502. <https://doi.org/10.1016/j.jchromb.2025.124502>
- 592 [23] WEI M, LI H, LI Q, QIAO Y, MA Q et al. Based on Network Pharmacology to Explore the  
593 Molecular Targets and Mechanisms of Gegen Qinlian Decoction for the Treatment of  
594 Ulcerative Colitis. *Biomed Res Int* 2020; 2020: 5217405.  
595 <https://doi.org/10.1155/2020/5217405>
- 596 [24] LI JD, FENG QC, QI Y, CUI G, ZHAO S. PPARGC1A is upregulated and facilitates lung  
597 cancer metastasis. *Exp Cell Res* 2017; 359: 356-360.  
598 <https://doi.org/10.1016/j.yexcr.2017.08.017>
- 599 [25] LIU R, WANG J, ZHANG L, WANG S, LI X et al. GLIDR-mediated regulation of tumor  
600 malignancy and cisplatin resistance in non-small cell lung cancer via the  
601 miR-342-5p/PPARGC1A axis. *BMC Cancer* 2024; 24: 1126.  
602 <https://doi.org/10.1186/s12885-024-12845-y>
- 603 [26] BAI X, SHAO J, DUAN T, LIU X, WANG M et al. Exo-miR-1290-induced by COX-2  
604 overexpression promotes cancer-associated fibroblasts activation and tumor progression by  
605 CUL3-Nrf2 pathway in lung adenocarcinoma. *Cell Commun Signal* 2023; 21: 242.  
606 <https://doi.org/10.1186/s12964-023-01268-0>
- 607 [27] SU L, CHEN Y, HUANG C, WU S, WANG X et al. Targeting Src reactivates pyroptosis to  
608 reverse chemoresistance in lung and pancreatic cancer models. *Sci Transl Med* 2023; 15:  
609 eabl7895. <https://doi.org/10.1126/scitranslmed.abl7895>
- 610 [28] POKHREL RH, ACHARYA S, AHN JH, GU Y, PANDIT M et al. AMPK promotes  
611 antitumor immunity by downregulating PD-1 in regulatory T cells via the HMGCR/p38  
612 signaling pathway. *Mol Cancer* 2021; 20: 133. <https://doi.org/10.1186/s12943-021-01420-9>
- 613 [29] ZENG Y, PAN Y, ZHANG B, LUO Y, TIAN J et al. Integrating Network Pharmacology,  
614 Molecular Docking, and Experimental Validation to Investigate the Mechanism of (-)-Guaiol  
615 Against Lung Adenocarcinoma. *Med Sci Monit* 2022; 28: e937131.  
616 <https://doi.org/10.12659/MSM.937131>

- 617 [30] ZHANG T, QIAN Y, YUAN C, WU Y, QIAN H et al. Propranolol Suppresses Proliferation  
618 and Migration of HUVECs through Regulation of the miR-206/VEGFA Axis. *Biomed Res*  
619 *Int* 2021; 2021: 7629176. <https://doi.org/10.1155/2021/7629176>
- 620 [31] ZHU Y, JIANG X, DING Z, MING J. Interleukin 7 inhibit autophagy via P53 regulated  
621 AMPK/mTOR signaling pathway in non-small cell lung cancer. *Sci Rep* 2022; 12: 11208.  
622 <https://doi.org/10.1038/s41598-022-14742-5>
- 623 [32] SHI L, XU Z, YANG Q, HUANG Y, GONG Y et al. IL-7-Mediated IL-7R-JAK3/STAT5  
624 signalling pathway contributes to chemotherapeutic sensitivity in non-small-cell lung cancer.  
625 *Cell Prolif* 2019; 52: e12699. <https://doi.org/10.1111/cpr.12699>
- 626 [33] ZHU MC, ZHANG YH, XIONG P, FAN XW, LI GL et al. Circ-GSK3B up-regulates  
627 GSK3B to suppress the progression of lung adenocarcinoma. *Cancer Gene Ther* 2022; 29:  
628 1761-1772. <https://doi.org/10.1038/s41417-022-00489-8>
- 629 [34] MAO W, YIN H, CHEN W, ZHAO T, WU S et al. Network Pharmacology and  
630 Experimental Evidence Reveal Dioscin Suppresses Proliferation, Invasion, and EMT via  
631 AKT/GSK3b/mTOR Signaling in Lung Adenocarcinoma. *Drug Des Devel Ther* 2020; 14:  
632 2135-2147. <https://doi.org/10.2147/DDDT.S249651>
- 633 [35] JIA L, LV D, ZHANG S, WANG Z, ZHOU B. Astragaloside IV Inhibits the Progression of  
634 Non-Small Cell Lung Cancer Through the Akt/GSK-3 $\beta$ /Catenin Pathway. *Oncol Res*  
635 2019; 27: 503-508. <https://doi.org/10.3727/096504018X15344989701565>
- 636 [36] ZHANG H, WANG Y, LU J, ZHAO Y. Long non-coding RNA LINC00222 regulates  
637 GSK3 $\beta$  activity and promotes cell apoptosis in lung adenocarcinoma. *Biomed Pharmacother*  
638 2018; 106: 755-762. <https://doi.org/10.1016/j.biopha.2018.06.165>
- 639 [37] Gao F, Yu X, Li M, Zhou L, Liu W et al. Deguelin suppresses non-small cell lung cancer by  
640 inhibiting EGFR signaling and promoting GSK3 $\beta$ /FBW7-mediated Mcl-1 destabilization.  
641 *Cell Death Dis* 2020; 11: 143. <https://doi.org/10.1038/s41419-020-2344-0>
- 642 [38] LIU XH, TANG DE, DAI Y, GAO XJ, LIU LX. PCNA and GSK3 $\beta$  interact with each other  
643 to regulate H1299 lung adenocarcinoma cells apoptosis. *Neoplasma* 2020; 67: 15-26.  
644 [https://doi.org/10.4149/neo\\_2019\\_190116N48](https://doi.org/10.4149/neo_2019_190116N48)
- 645 [39] XIONG M, LIU D, WANG X, REN H, CHI W et al. PPARG Activation of Fatty Acid  
646 Metabolism Drives Resistance to Anti-HER2 Therapies in HER2-Positive Breast Cancer. *Int*  
647 *J Biol Sci* 2025; 21: 2396-2414. <https://doi.org/10.7150/ijbs.99275>
- 648 [40] JIANG S, LI H, ZHANG L, MU W, ZHANG Y et al. Generic Diagramming Platform  
649 (GDP): a comprehensive database of high-quality biomedical graphics. *Nucleic Acids Res*  
650 2025; 53: D1670-D1676. <https://doi.org/10.1093/nar/gkae973>

651

## 652 **Figure Legends**

653

654 **Figure 1.** The common targets between (-)-Guaiol and lung cancer screened by Network  
655 Pharmacology. A) Venn diagram showing the targets of the component-disease intersection. B) PPI  
656 network diagram of common potential targets between (-)-Guaiol and lung cancer. C) Network  
657 diagram of (-)-Guaiol interaction with key targets in lung cancer.

658

659 **Figure 2.** Go and KEGG enrichment analysis results. A) Histogram of the top 20 entries in the GO  
660 function enrichment analysis of genes. B) Bubble chart of top 20 Degree entries as a result of GO  
661 functional enrichment analysis. C) Bubble plot of TOP20 Degree entries from KEGG enrichment  
662 analysis results.

663

664 **Figure 3.** Network of relationships between (-)-Guaioi, key targets, Top20 KEGG pathways and  
665 lung cancer.

666

667 **Figure 4.** Molecular docking of (-)-Guaioi with key targets. A) (-)-Guaioi-ESR1; B)  
668 (-)-Guaioi-EGFR; C) (-)-Guaioi-PPARG; D) (-)-Guaioi-PTGS2; E) (-)-Guaioi-HSP90AA1; F)  
669 (-)-Guaioi- src; G) (-)-Guaioi-GSK3B.

670

671 **Figure 5.** Molecular dynamics simulation of the protein-ligand complex. A) Root-mean-square  
672 deviation (RMSD) values of the protein-ligand complex over time; B) Radius of gyration (Rg)  
673 values of the protein-ligand complex over time; C) Solvent-accessible surface area (SASA) values  
674 of the protein-ligand complex over time; D) Number of hydrogen bonds (HBonds) in the  
675 protein-ligand complex over time; E) Root-mean-square fluctuation (RMSF) values of the protein-  
676 ligand complex.

677

678 **Figure 6.** MMPBSA binding free energy calculation. A) binding free energy; B-H) the amino acid  
679 residues that contributed significantly to the binding of the small molecule within each complex  
680 system.

681

682 **Figure 7.** mRNA sequencing results. A) Differential gene expression level clustering analysis. B)  
683 WikiPathways enrichment analysis and chord plot. C) WikiPathways enrichment analysis.

684

685 **Figure 8.** (-)-Guaioi inhibits cell proliferation and invasion ability of lung cancer cells. A) IC50  
686 value of (-)-Guaioi on A549 cells and H1299 cells. B) Western Blot to detect the effect of (-)-Guaioi  
687 on PPARG and its downstream related proteins in A549 cells and H1299 cells. C) Plate cloning  
688 experiment to verify the effect of (-)-Guaioi on A549 cells' capacity for proliferation. D) Wound

689 healing experiments to verify the effect of (-)-Guaiol on migration ability in A549 cells. E)  
690 Transwell assay to verify the effect of (-)-Guaiol on invasion ability in A549 cells. Control group  
691 received 0.1% DMSO (vehicle). All treatments were normalized to equivalent solvent  
692 concentration.

693

694 **Figure 9.** (-)-Guaiol inhibits the growth of transplanted tumors in lung cancer subcutaneous  
695 xenograft mice. A) Subcutaneous tumor peeling photographed. B) Mouse body weight change curve.  
696 C) Transplanted tumor tumor volume change curve. D) Mouse tumor mass scatter plot. E)  
697 Immunohistochemical results of subcutaneous graft tumors in mice after treatment with (-)-Guaiol  
698 action.

699

700 **Figure 10.** Sketch of the mechanism by which (-)-Guaiol modulates the PPARG signaling pathway  
701 to inhibit lung cancer.

Accepted manuscript

Fig. 1 [Download full resolution image](#)

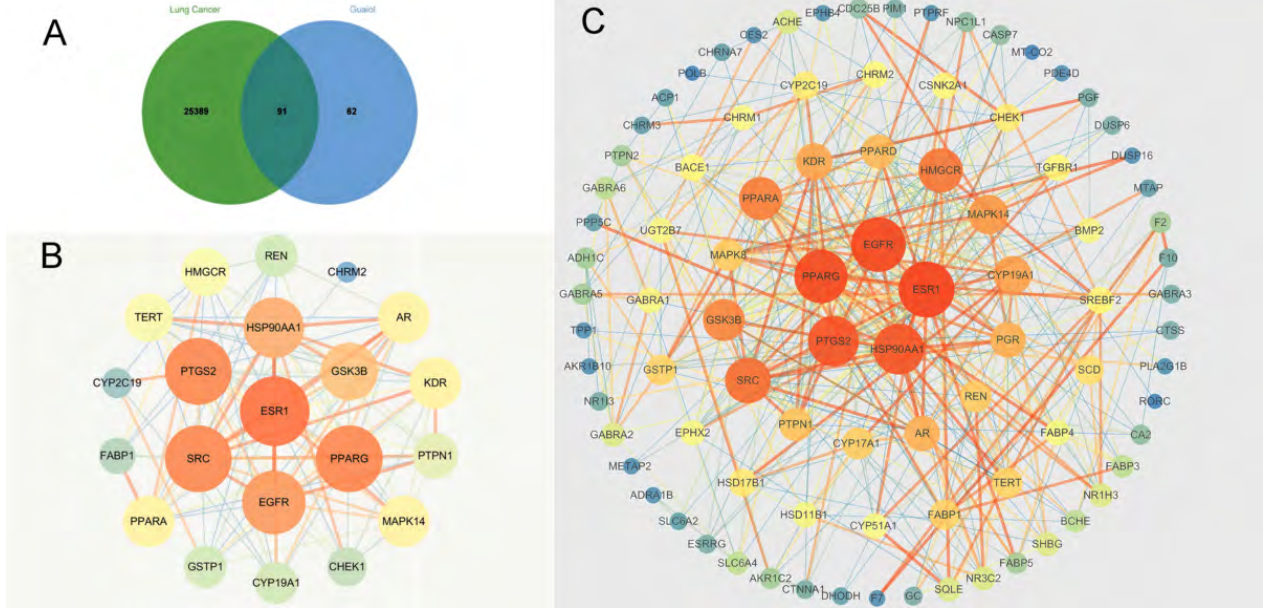


Fig. 2 [Download full resolution image](#)

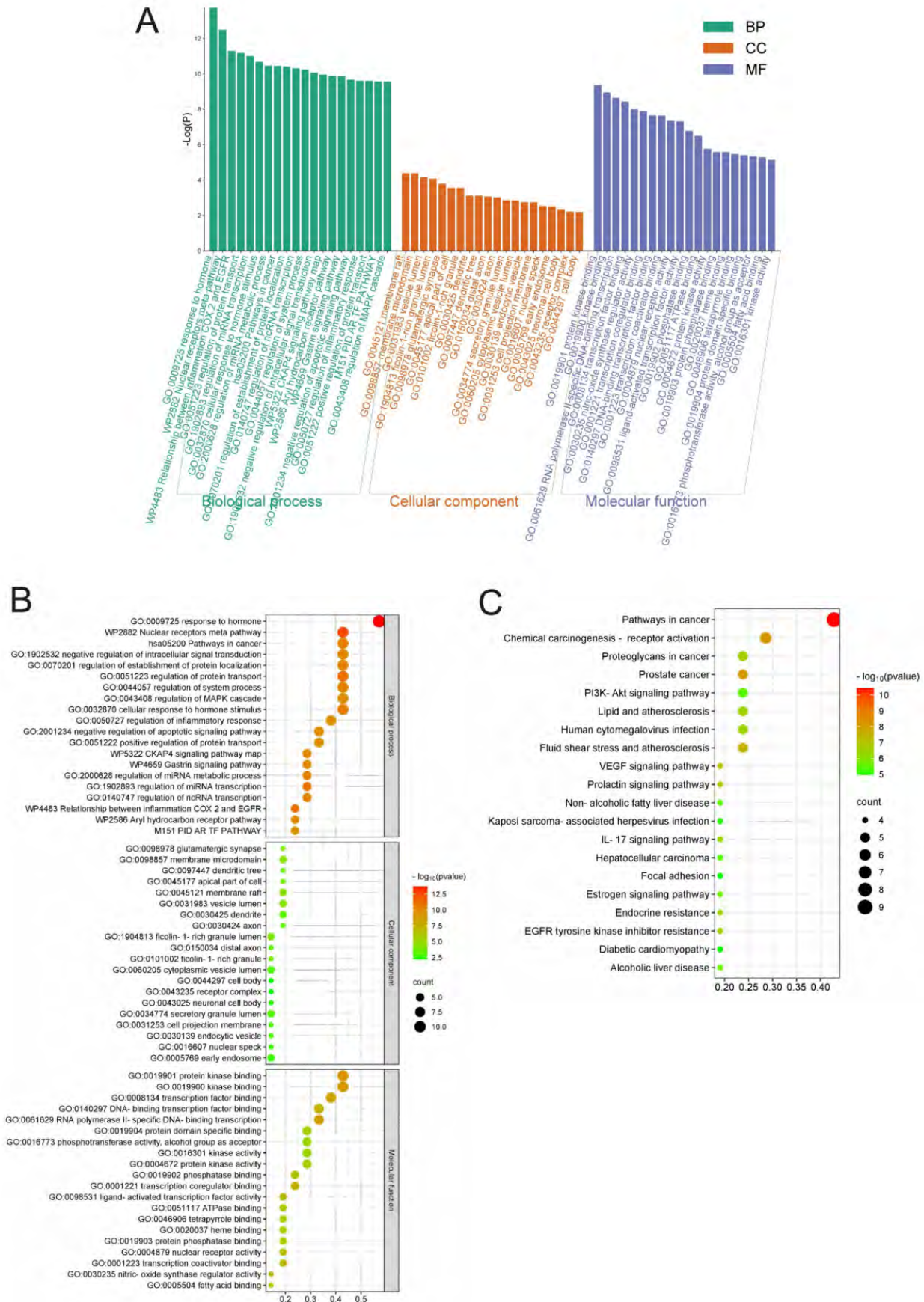


Fig. 3 [Download full resolution image](#)

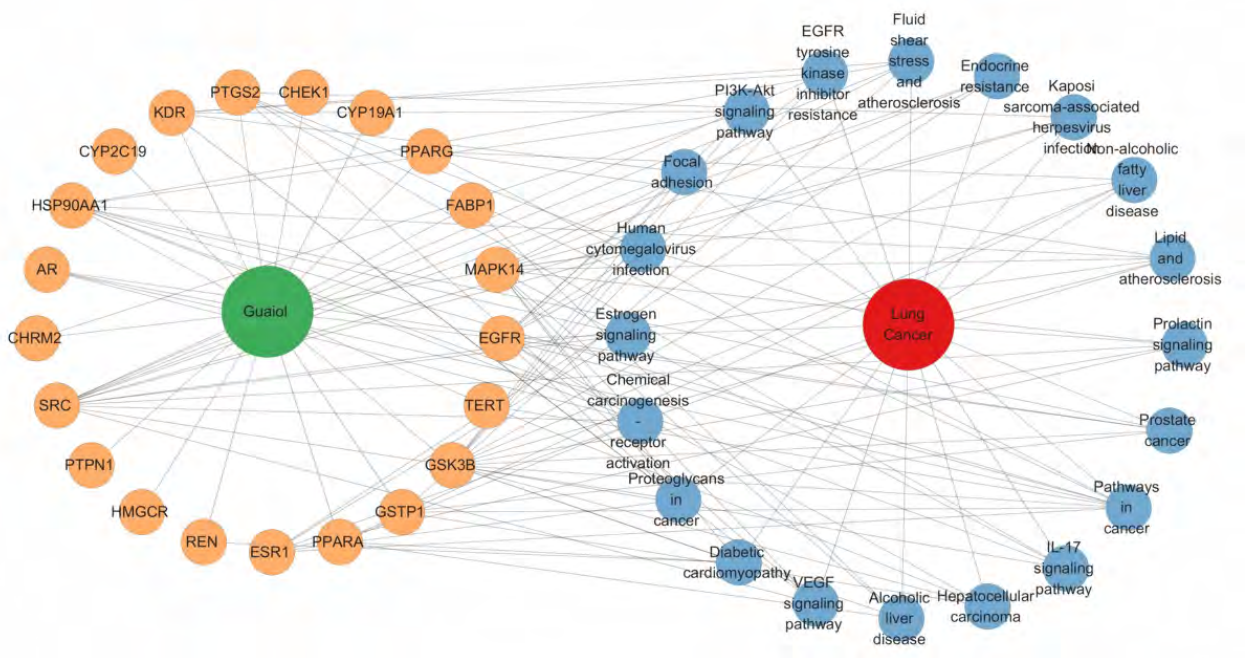




Fig. 5 [Download full resolution image](#)

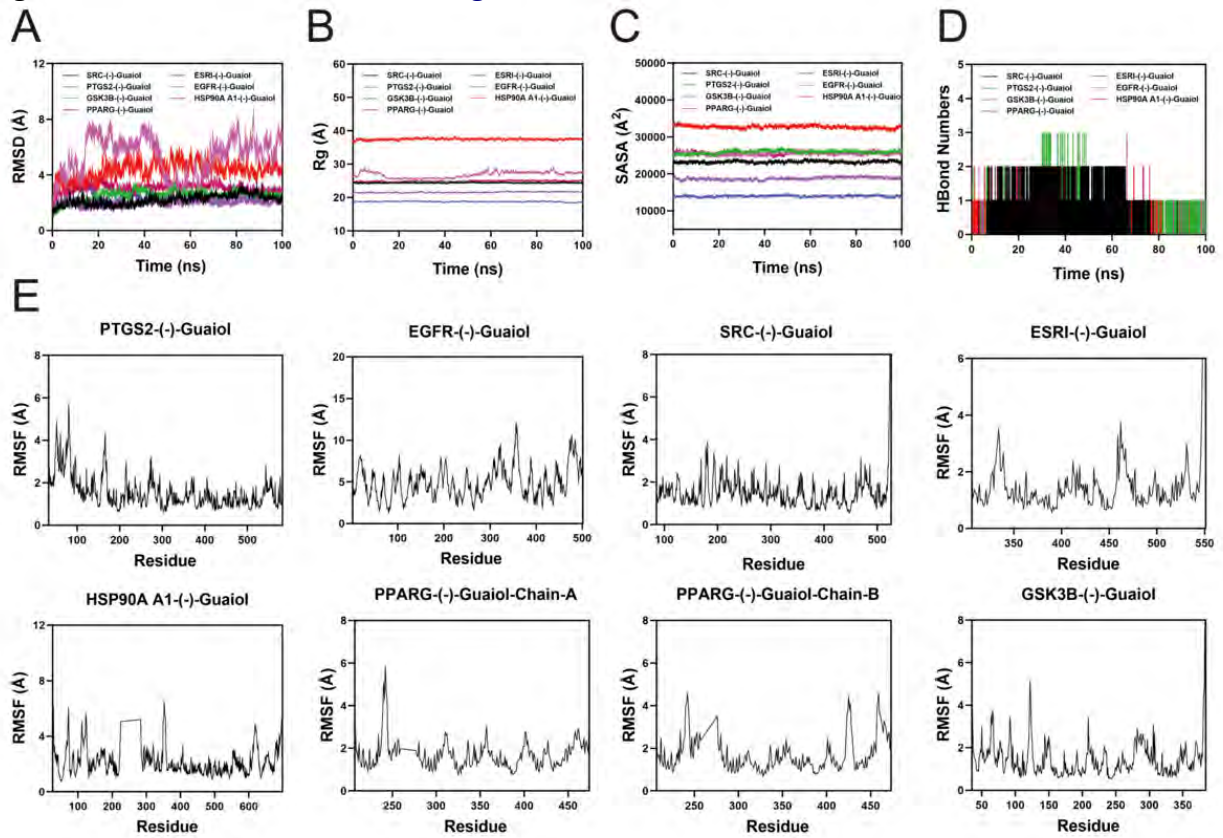
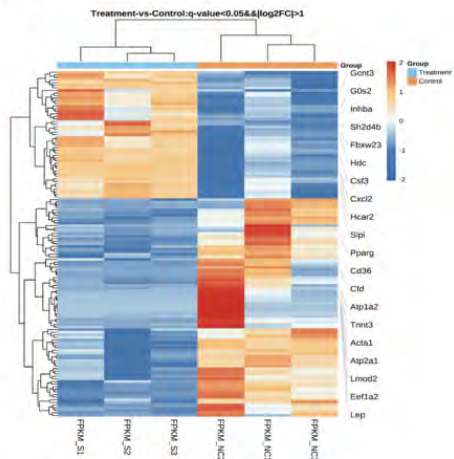


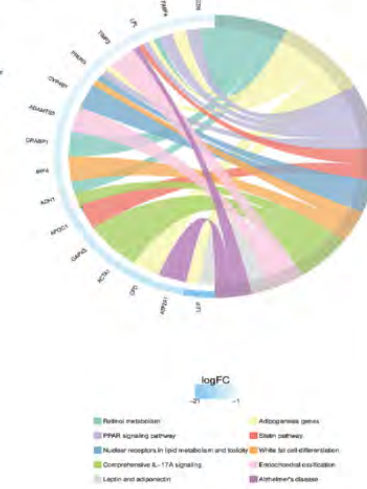


Fig. 7 [Download full resolution image](#)

A



B



C



Fig. 8 [Download full resolution image](#)

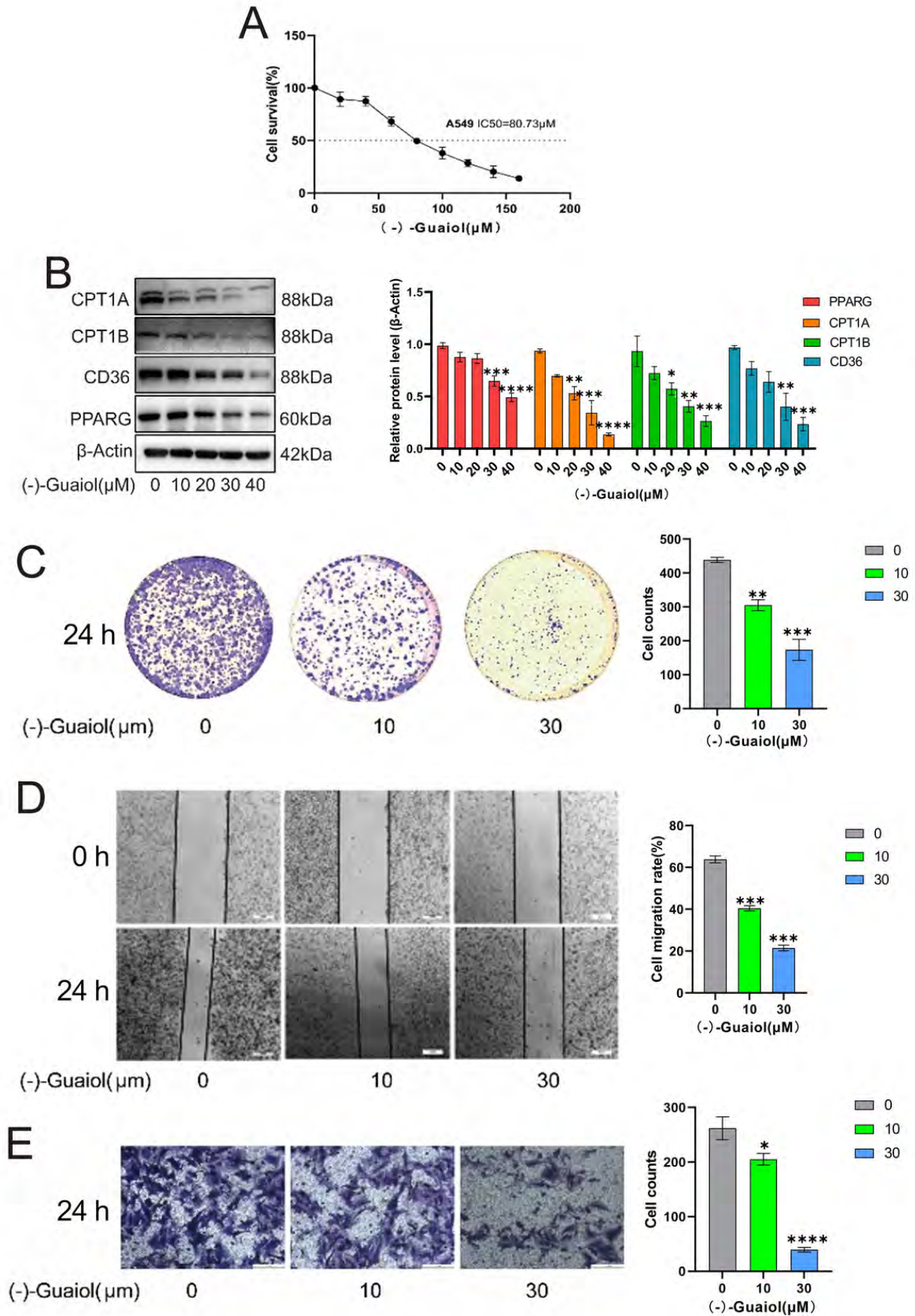


Fig. 9 [Download full resolution image](#)

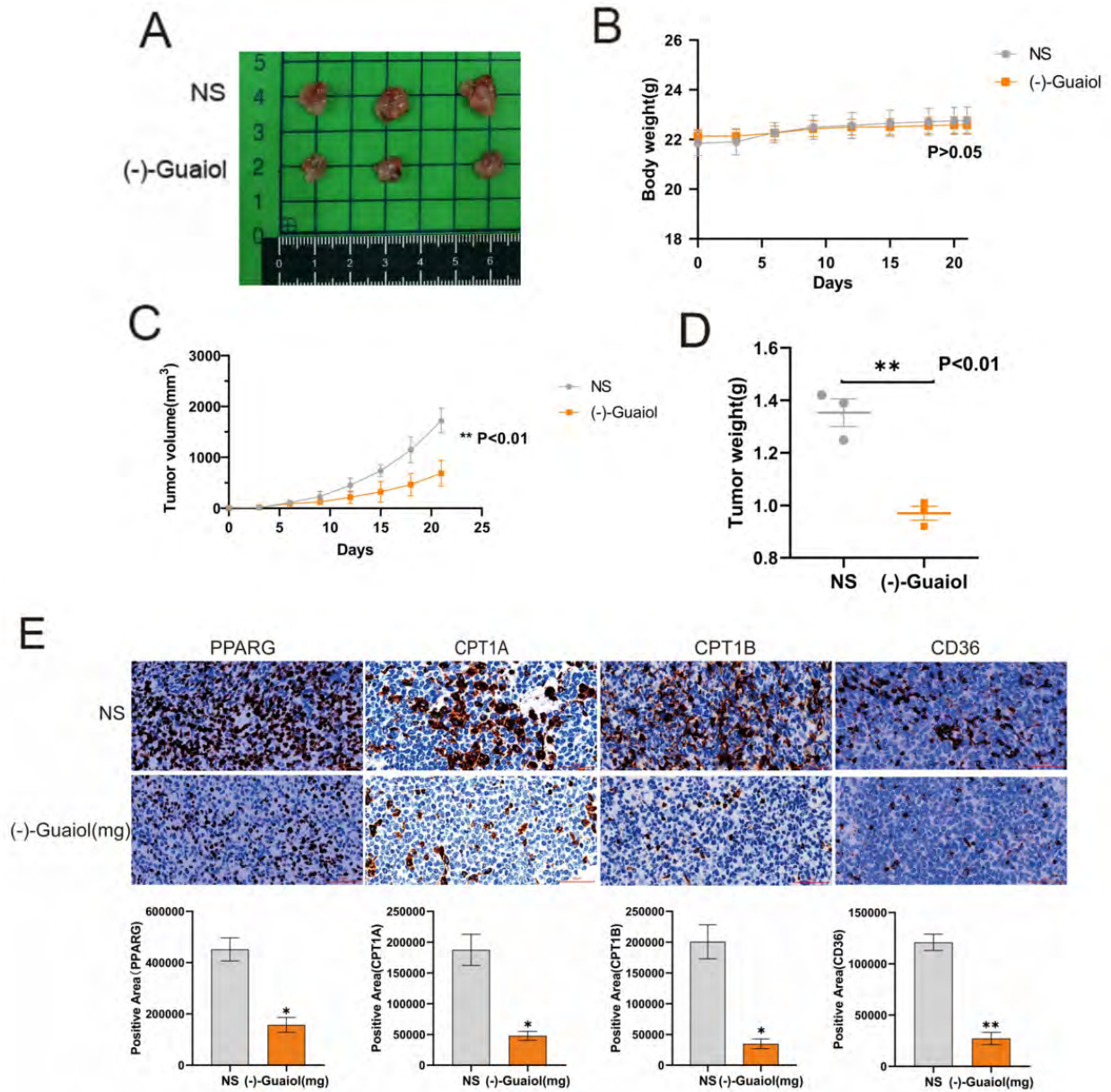


Fig. 10 [Download full resolution image](#)

